Available online at www.sciencedirect.com
ScienceDirect
Trans. Nonferrous Met. Soc. China 29(2019) 1665−1676
Transactions of Nonferrous Metals Society of China
www.tnmsc.cn

# Laser in-situ synthesis of titanium matrix composite coating with TiB−Ti network-like structure reinforcement

Ying-hua LIN[1], Zhen-heng LIN[1], Qing-tang CHEN[1], Yong-ping LEI[1,2], Han-guang FU[2]

1. School of Mechanical and Electrical Engineering, Putian University, Putian 351100, China;
2. College of Materials Science and Engineering, Beijing University of Technology, Beijing 100124, China

Received 15 October 2018; accepted 19 April 2019

**Abstract:** To avoid high crack sensitivity of TiB−Ti composite coating during laser cladding process, network-like structure composite coating was fabricated with laser in-situ technique on titanium alloy using 5 μm $TiB_2$ powder as the cladding material. The microstructure, phase structure and properties of the coatings were analyzed by SEM, XRD, EPMA, TEM, hardness tester and fretting wear meter. It was observed that the outer ring of the network-like structure was mainly TiB strengthening phase, while the inner ring was $\alpha$-Ti grain, and the interface between TiB and Ti matrix was very clean and had a consistent orientation relationship. The hardness of the cladding layer with network-like structure gradually decreased from the surface toward the interface, but the average hardness was nearly two times that of the substrate. In the fretting wear test, it was found that the wear resistance of the cladding layer with network-like structure was larger than that of the substrate under low load (40 N). The results revealed that the hardness and fretting wear resistance of the titanium-based composite coating could be improved by the introduction of network-like structure.

**Key words:** laser cladding forming; titanium matrix composite coating; TiB−Ti; fretting wear

## 1 Introduction

Titanium alloy is widely used to replace steel for various parts of aeroengines due to its low density, high specific strength and good corrosion resistance. However, the reliability of titanium alloy is greatly affected by its high coefficient of friction and severe adhesive wear, especially in fretting wear [1,2]. TiB short fiber has many attractive attributes, such as high elastic modulus, high hardness and high wear resistance. Meanwhile, the compatibility and stability of TiB particles in Ti matrix are very good [3]. Moreover, the density and thermal expansion coefficient of TiB and Ti are very similar, which can reduce the residual stress in the composite [4]. In the past, researchers had always pursued uniform distribution of TiB-reinforced phase in the Ti matrix [5−7]. In recent years, HUANG et al [8] found that TiB network structure reinforced titanium matrix composites can be prepared with low energy ball milling and hot pressing sintering technology. The plasticity of TiB network structure material was five times higher than that of the uniform phase distribution material, and the strengthening effect of TiB network structure material can also be improved.

The network structure refers to a capsule-like structure in which the strengthening phase is uniformly distributed within the matrix. Its remarkable feature is that the strengthening phase in the accumulation area has macro continuity and the reinforcing phase of the network interface does not form complete connection. In this network structure, the reinforcing phase at the network interface does not form a complete connection, so that the plastic characteristic of the network can be exerted. The interior of the network structure can effectively hinder crack nucleation and crack propagation. Compared with the uniform distribution of the traditional reinforcement phase, the splitting effect of the reinforcing phase can be greatly reduced. Therefore, the crack sensitivity of the network structure can be greatly reduced [9,10]. In addition, the network structure can exhibit high temperature softening resistance. In

**Foundation item:** Projects (2019J01813, 2018J01557) supported by the Natural Science Foundation of Fujian Province, China; Project (2018H0031) supported by the Guiding Science Program of Fujian Province, China; Project (2018GP2002) supported by the Science and Technology Program of Putian City, China

**Corresponding author:** Yong-ping LEI; Tel: +86-594-2692440; Fax: +86-594-2692367; E-mail: lyh351258@126.com

DOI: 10.1016/S1003-6326(19)65073-9

order to obtain good mechanical properties of TiB network structure prepared using conventional method, subsequent thermal deformation or heat treatment is required [8,11]. Additionally, porosity of the network structure is hardly eliminated [12,13]. In recent years, laser cladding technology has gradually become an important means for surface modification and repair of titanium alloys due to the advantages of dense microstructure, good metallurgical bonding between the coating and substrate and low substrate heat effect [14,15]. HU et al [16] found that network structure composite coating can be prepared with laser technique using large particle size Ti powder and small particle size B powder as cladding materials. The microstructure of network structure was dense, and the obtained coating exhibited excellent mechanical properties and wear resistance. However, since both $TiB_2$ and TiB were formed using laser in-situ technique when Ti powder and B powder were cladding materials, and the reaction driving force of $TiB_2$ was greater than that of TiB, it was difficult to achieve large-area TiB network composites.

At present, an effective way to obtain TiB is to utilize in-situ reaction between Ti element and B element. The main materials for providing B element are $B_4C$, BN, $TiB_2$ and B powder [16−19], but both TiB and $TiB_2$ can be formed by in-situ reaction between $B_4C$, BN, B powder and Ti powder. The formation conditions are not easily controlled, and the repeatability of experiments is poor, which makes the composite material difficult to meet various needs of research and application. Density and thermal expansion coefficient among $TiB_2$ and TiB and Ti can be very similar [20], only when TiB was formed by in-situ reaction between $TiB_2$ and Ti, which was favorable for obtaining high stability and high quality TiB reinforced titanium matrix composite. Therefore, in the present study, network-like structure composite coating was fabricated with laser in-situ technique on the surface of titanium alloy substrate using $TiB_2$ powder as the cladding material, and the formation mechanism and the properties of the network-like structure were investigated.

## 2 Experimental

### 2.1 Material preparation

TC4 titanium alloy was selected as the substrate material. The substrate specimen had a diameter of 300 mm and a length of 15 mm. The pre-coated layer material was pure $TiB_2$ powder (purity of 99.5%, and average grain size of 5 μm). A proper amount of 2123 phenolic resin was used as a binder, and pure $TiB_2$ powder was placed on the surface of the specimen with pre-coated layer thickness of 0.2 mm. The pre-coated layer was dried in a vacuum oven at 120 °C for 60 min. Laser cladding was performed using YLS−6000 IPG fiber laser under the condition of Ar gas-protected molten pool with a flow rate of 15 L/h. Process parameters of laser cladding were selected as follows: laser power was 1.0−3.0 kW, scanning velocity was 4−10 mm/s and square spot size was 5 mm × 5 mm.

### 2.2 Microstructure characterization

After laser cladding, the coating specimen was wire-cut, ground, polished, and etched with an etchant of $V(HNO_3):V(HF):V(H_2O)$=3:2:95. The microstructure of the coating was examined using a JSM−6490LA scanning electron microscope (SEM). The phase of the cladding layer was analyzed using a D/max 2550 VL/PC type X-ray diffractometer (XRD). The elemental contents of the microstructure were analyzed using a JXA−8100 electron probe (EPMA). The fine structure of the sample was investigated using a JEOL−2100 transmission electron microscope (TEM) at a working voltage of 200 kV, and the zone axis and orientation relationship of the phase was determined by selected area electron diffraction (SAED).

### 2.3 Performance evaluation

The micro-hardness of the cladding layer and the substrate was measured using a HXD−1000B micro-hardness tester with an indentation load of 1.96 N and dwell time of 15 s. The fracture toughness of the cladding layer was investigated using an HBV−187.5 electric Bllov hardness tester. According to the theory of indentation fracture mechanics [21], only driving force for crack propagation was the residual stress caused by the elasto-plastic deformation of the indentation tip. Thus, indentation was made on the polished cladding layer using an FM−700 digital micro-hardness tester with a loading load of 30 kg and a holding time of 15 s. The fretting wear test was performed using the microvibration friction and wear tester (FTM200). The contact of fretting wear was the mode of line−surface contact, and the schematic diagram of the test mode is shown in Fig. 1. Detailed material data and experimental parameters are given in Tables 1 and 2. The worn surface morphology was analyzed using scanning electron microscopy (SEM). The wear losses of the cladding layer and the substrate were measured using a Mahr-M1 profilometer.

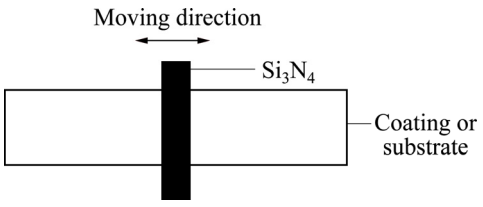


**Fig. 1** Schematic diagram of fretting wear tester

## 3 Results and discussion

### 3.1 Network-like structure characterization

Figure 2 shows the SEM images of the laser claddings with 5 μm $TiB_2$ reinforcement in transverse cross-section prepared at a laser power of 2.0 kW and scan speed of 6 mm/s with pre-coated layer thickness of 0.2 mm. First, no cracks and pores were observed in the cladding layer. Second, a good metallurgical bond between the cladding layer and the substrate was formed (Fig. 2(a)). Third, the network-like structure of the cladding layer was achieved, and the spatial length gradually increased from the cladding layer surface to the interface. By careful observation, it was found that the network-like structure of the top and the middle of the layer was mainly composed of particles and fine needles, and the average size of the particles was 1−3 μm, the length and the diameter of the fine needles were 4−7 μm and 300−500 nm, respectively. The average spatial lengths of the network-like structure of the top and the middle of the layer were about 4 and 7 μm, respectively. However, the network-like structure of the bottom was composed of fine needles, and the length and diameter of the fine needles were nearly the same as those at the top and middle of the layer, but the average spatial length of the network-like structure increased to 10 μm.

Since B was an element with a low atomic number, the content of B element was difficult to be quantified accurately using energy spectrum (EDS). Therefore, the phases of the coating were analyzed by the combination of XRD and EPMA. Figure 3 shows the XRD spectrum of the cladding layer and the areas at the top and the bottom of the coating for analysis. It can be seen that the cladding layer was mainly composed of $\alpha$-Ti, orthorhombic structure TiB, a small amount of $\beta$-Ti and body-centered cubic (bcc) structure TiB. From statistics

**Table 1** $Si_3N_4$ material data

| Rod diameter/mm | Rod length/mm | Rod roughness/μm | Elastic modulus/MPa | Fracture toughness/(MPa·m$^{3/2}$) | Hardness (HV) |
|---|---|---|---|---|---|
| 6 | 10 | ＜0.8 | 30−32 | 4.5 | 1500−1800 |

**Table 2** Fretting wear test parameters

| Test temperature/℃ | Load/N | Frequency/Hz | Amplitude/μm | Time/min | Sample size |
|---|---|---|---|---|---|
| 23−30 | 40, 80 | 20 | 100 | 30 | 12 mm × 20 mm × 10 mm |

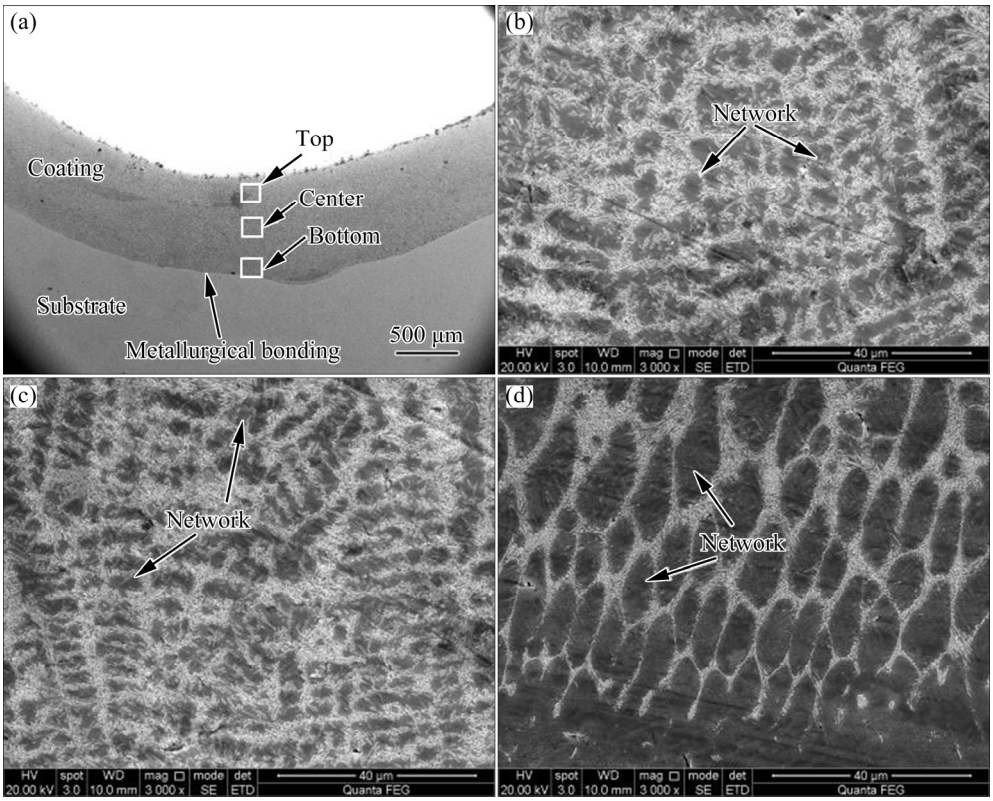


**Fig. 2** SEM images of cladding layer at laser power of 2.0 kW, scanning speed of 6 mm/s and pre-coated layer thickness of 0.2 mm: (a) Macro-shape; (b) Top; (c) Center; (d) Bottom

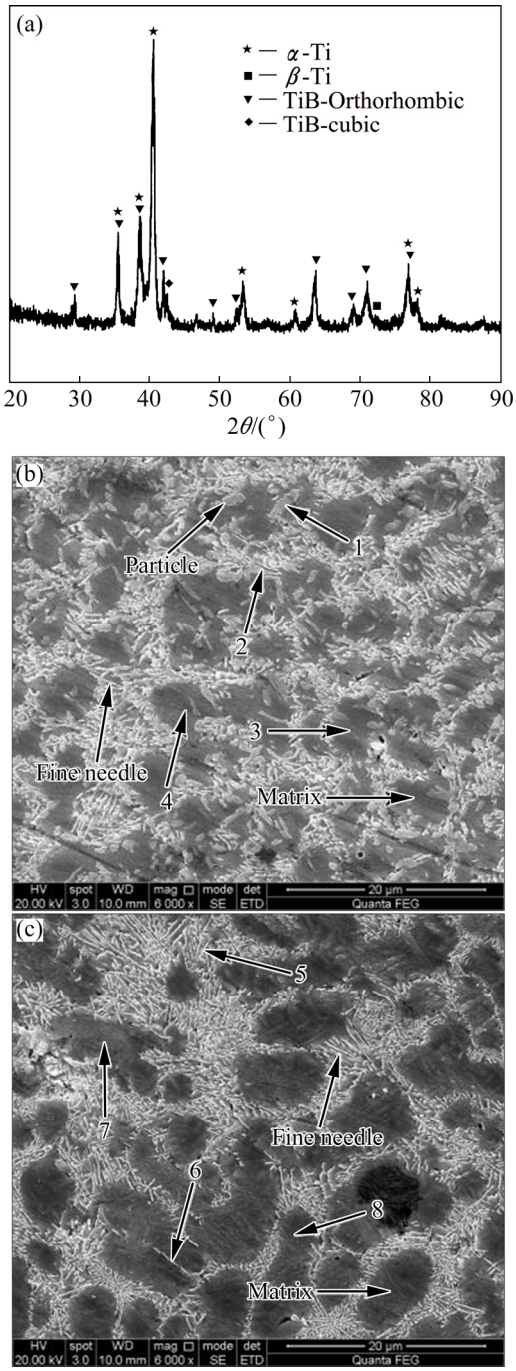


**Fig. 3** XRD spectrum (a) and EPMA composition analysis areas at top (b) and bottom (c) of cladding layer

combined with XRD analysis, it was confirmed that both the particle and the fine needles were TiB phases, and the results were summarized in Table 3. By comparing the XRD spectrum with the standard peak positions, it can be found that the positions of some diffraction peaks were significantly shifted, e.g., the TiB diffraction peaks of 29.5°, 42.8°, and 63.4° were shifted to the right. The reason for this was insufficient diffusion of the elements in the micro-region, due to rapid melting and rapid cooling by laser, which caused solid solution of Al and V elements in the nucleation process of TiB phase (Table 3), resulting in lattice distortion. This was consistent with the XRD results. Meanwhile, it can be seen from Table 3 that Area 3 and Area 4 were selected to analyze Ti matrix at the top and Ti matrix of the region containing high content of Al element, which favored the stability of $\alpha$-Ti. Area 7 and Area 8 were selected to measure Ti matrix at the bottom, and Ti matrix of the region containing high content of V element, which favored the stability of $\beta$-Ti. From statistics analyses, it was found that the contents of Al and V elements at the top and the bottom of the coating were different. Because the density of Al was 2.7 g/cm$^3$, the density of V was 6.11 g/cm$^3$, and the density of Ti was 4.50 g/cm$^3$, which was just between the densities of Al element and the V element, the V element hardly floated up to the top in the laser cladding process due to its high density, while Al element easily floated up because of its low density. Therefore, the content of $\beta$-Ti at the bottom of the coating was greater than that at the top.

**Table 3** Elemental contents analyzed by EPMA (at.%)

| Position | Ti | B | Al | V |
|---|---|---|---|---|
| 1 | 55.6 | 42.8 | 0.9 | 0.7 |
| 2 | 57.5 | 41.3 | 0.8 | 0.4 |
| 3 | 95.4 | 3.8 | 0.6 | 0.2 |
| 4 | 94.7 | 4.1 | 0.7 | 0.5 |
| 5 | 54.3 | 44.2 | 0.7 | 0.8 |
| 6 | 56.8 | 41.6 | 1.0 | 0.6 |
| 7 | 92.1 | 6.7 | 0.9 | 0.3 |
| 8 | 94.3 | 4.9 | 0.3 | 0.5 |

Figure 4 shows fine structure of TiB−Ti under TEM. It can be seen that the morphology of TiB was needle-like, but not completely regular. The diameter of the tip was reduced, compared with the middle, and the average diameter was gradually reduced from 0.5 to 0.3 μm. The interface between TiB and Ti matrix was very clean in most areas. The matrix phase around TiB included $\beta$-Ti and $\alpha$-Ti. The morphology of $\alpha$-Ti in the network-like structure was mainly in a long strip arrangement, and the morphology of $\beta$-Ti at the interface between $\alpha$-Ti and TiB was more irregular. The number and the size of $\beta$-Ti were significantly less than those of $\alpha$-Ti, as shown in Fig. 4(e). The primary $\beta$-Ti can be transformed into secondary $\alpha$-Ti, and the position of $\beta$-Ti phase would be gradually occupied by $\alpha$-Ti. Finally, only a small amount of $\beta$-Ti would remain at the secondary $\alpha$-Ti grain boundary, and thus, the morphology of $\beta$-Ti was also irregular. This indicated that the Ti matrix formed in the network-like structure was mainly $\alpha$-Ti,

which was consistent with the XRD results.

In order to further verify the microstructural analyses, the fine structure of TiB/Ti was studied with a high resolution transmission electron microscopy (HRTEM), as shown in Fig. 5. It can be seen more clearly that the interface between TiB and Ti matrix was very clean without any intermediate impurity phase, the thickness of the transition zone was only 2−3 nm (Fig. 5(a) and Fig. 5(b)), and the interface had a coherent structure observed by HRTEM. The internal structure of

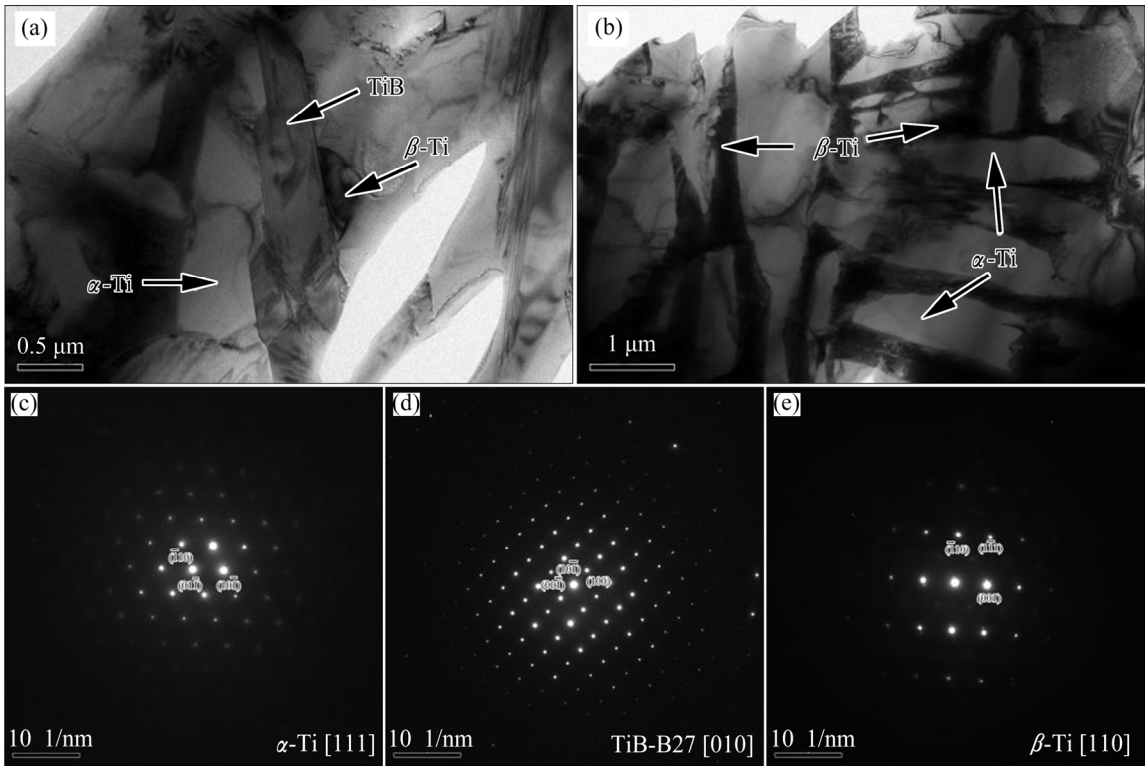


**Fig. 4** TEM observation of TiB−Ti: (a) Bright field images of TiB, $\alpha$-Ti and $\beta$-Ti; (b) Morphology of different Ti matrix structures; (c) Electron diffraction pattern of $\alpha$-Ti; (d) Electron diffraction pattern of TiB; (e) Electron diffraction pattern of $\beta$-Ti

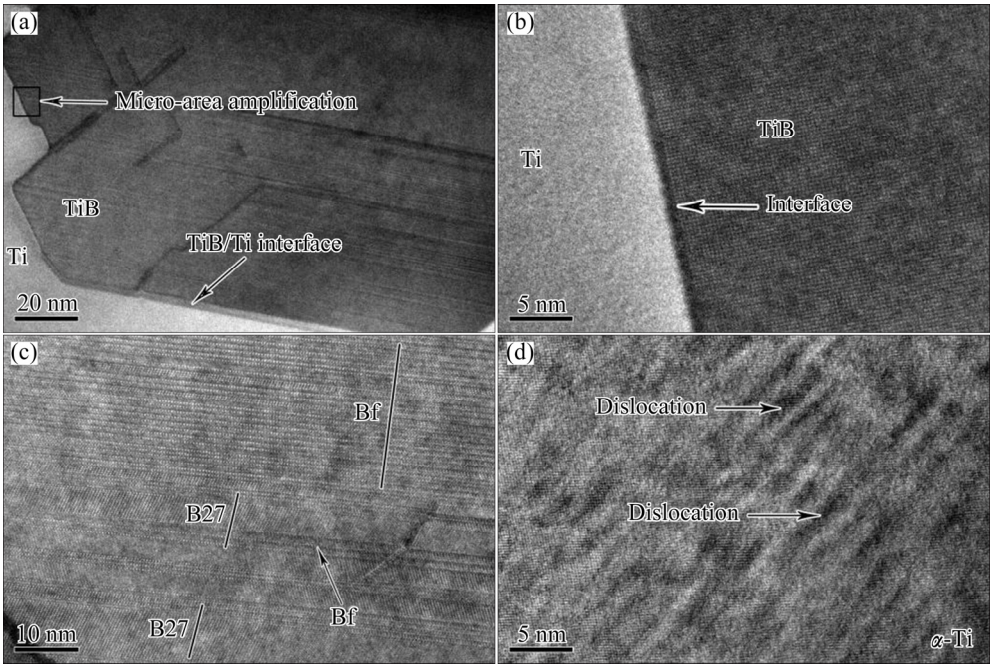


**Fig. 5** HRTEM images of TiB/Ti: (a) TiB/Ti interface at low magnification; (b) TiB/Ti interface at high magnification; (c) TiB internal structure; (d) $\alpha$-Ti internal dislocation

TiB can be divided into B27 and Bf structures (Fig. 5(c)). By examining multiple areas, it was found that these two structures had no fixed position in the TiB grains, and instead, they can occupy the inner region of the TiB grains, or they can be present only at the corners of the TiB grains. The proportion of the two structures was random, and either B27 structure or Bf structure can be dominant. The previous research [22] proved that $TiB_{Bf}$ was a metastable phase. As the laser process proceeded, $TiB_{Bf}$ would transform into $TiB_{B27}$, and finally, B27 was the main structure. However, TiB in the network-like structure was not completely transferred into B27 steady-state structure. Therefore, the morphology of TiB would not be completely needle-like. Meanwhile, the orientation relationship between TiB and Ti was determined by the tilting angle of the zone axis, as presented in Fig. 6 and Table 4. It can be seen that the fixed orientation relationship among $\alpha$-Ti, B27 and Bf exists. By statistics analyses, it was found that the probability of this orientation relationship in the network-like structure was very high, which was beneficial to improving the interfacial bonding strength between TiB and Ti matrix [23,24]. Moreover, the interior of the Ti matrix also contained a large number of dislocations (Fig. 5(d)), which were formed mainly due to plastic deformation of the Ti matrix during solidification of the molten pool. These dislocations were beneficial for further strengthening of the cladding layer.

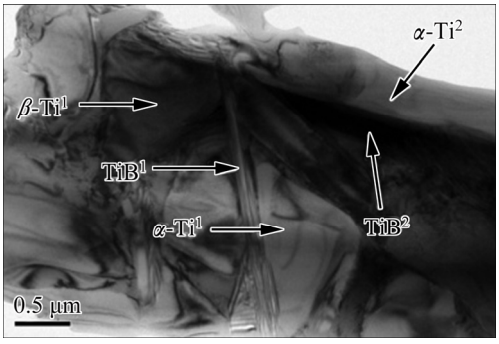


**Fig. 6** Image showing phases of TiB and Ti

**Table 4** Orientation relationship between TiB and Ti

| Phase | $T_x$/(°) | $T_y$/(°) | Zone axis | Angle/(°) |
|---|---|---|---|---|
| $TiB^1$ | −4.7 | −8.4 | $[001]_{Bf}$ | 0 |
| $TiB^2$ | −5.9 | 4.1 | $[010]_{B27}$ | 0 |
| $\alpha$-$Ti^1$ | −4.7 | −8.4 | $[11\bar{2}0]$ | 0 |
| $\alpha$-$Ti^2$ | −6.7 | −3.2 | $[01\bar{1}1]$ | 1.20 |
| $\beta$-$Ti^1$ | 0.4 | −5.4 | [111] | 0 |

### 3.2 Effects of laser process parameters on microstructure of cladding layer

In order to discover the formation conditions of the network-like structure, the effects of laser process parameters on the microstructure evolution during the laser pool solidification were studied. Figure 7 shows the SEM images of the middle of the cladding layer produced at a scanning speed of 6 mm/s under different laser powers with pre-coated layer of 0.2 mm in thickness. When the laser power was 1.5 kW, the cladding layer was mainly composed of $TiB_2$ particles (Fig. 7(a)), and the size of the particles was almost the same as that of the original powder, which implied that

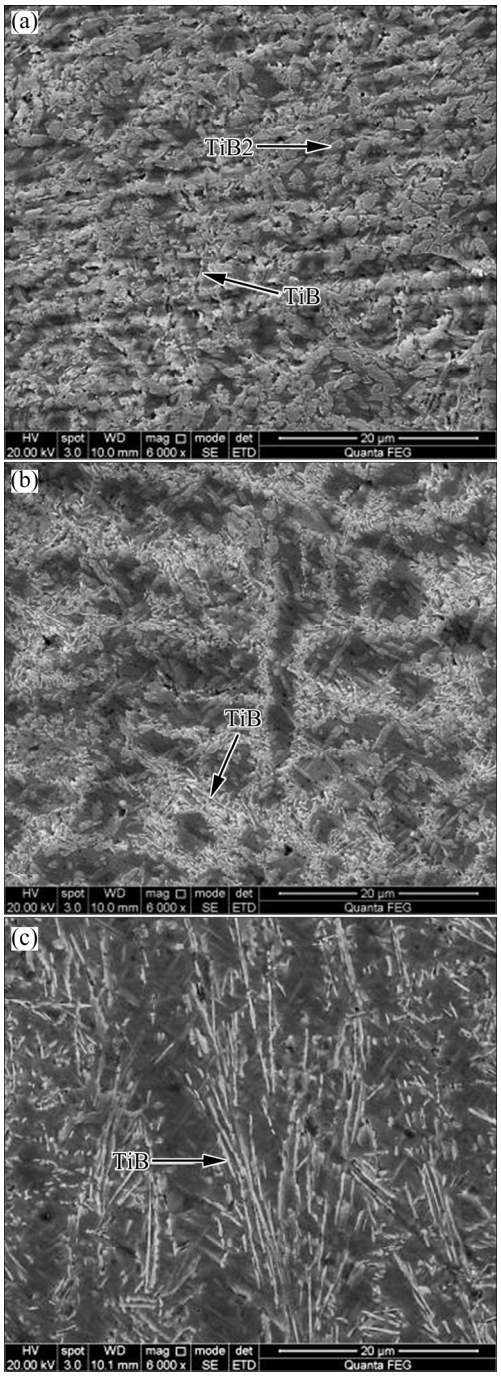


**Fig. 7** SEM images of middle of cladding layer at scanning speed of 6 mm/s and pre-coated layer thickness of 0.2 mm under different laser power: (a) 1.5 kW; (B) 2.0 kW; (c) 2.5 kW

the $TiB_2$ particles were not melted or dissolved under a lower laser energy density, and the in-situ reaction between $TiB_2$ and Ti hardly occurred. Network-like structure was formed in the cladding layer with the increasing of laser power (Fig. 7(b)), and the structure was mainly composed of fine needles and particles. It was found that both of fine needles and particles were TiB. With further increase of the laser power (Fig. 7(c)), it was found that the length of the fine needles became long, but the network-like structure was not formed. Figure 8 shows the SEM images of the middle of the cladding layer under the laser power of 2.0 kW at different scanning speeds with pre-coated layer of 0.2 mm in thickness. When the scanning speed was 8 mm/s, the cladding layer was mainly composed of $TiB_2$ particles and a small amount of TiB fine needles (Fig. 8(a)). With the increase of the scanning speed (10 mm/s), the cladding layer was mainly composed of $TiB_2$ particles (Fig. 8(b)). The network-like structure of the cladding layer was not found under these two conditions. Therefore, it can be inferred that formation of the network-like structure required an increase of the dissolved amount of $TiB_2$ particles, that is, residual $TiB_2$ in the cladding layer needed to be eliminated.

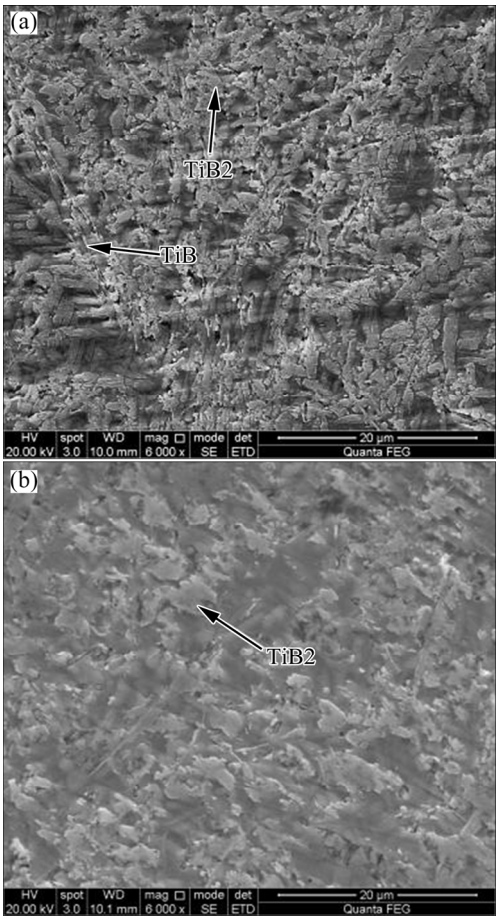


**Fig. 8** SEM images of middle of cladding layer at laser power of 2.0 kW and pre-coated layer thickness of 0.2 mm under different scanning speeds: (a) 8 mm/s; (b) 10 mm/s

## 4 Formation mechanisms of network-like structure during solidification of laser melting pool

The morphology and the distribution of the reinforcement in the cladding layer were directly related to the thermodynamic and kinetic conditions during the solidification process of the molten pool. The reaction mechanisms of in-situ synthesis of reinforcements mainly involved liquid−solid diffusion mechanism and dissolution−precipitation mechanism [25,26]. In this study, TiB reinforcement was formed by in-situ reaction between $TiB_2$ and Ti [27]. According to the analysis of the microstructure evolution, the network-like structure cannot be formed when the $TiB_2$ particles were not melted or dissolved (Fig. 7(a) and Fig. 8), which indicated that the key to the formation of the network-like structure was to eliminate residual $TiB_2$ particles in the cladding layer. However, removal of $TiB_2$ particles in the cladding layer was not guaranteed to form a network-like structure (Fig. 7(c)), which indicated that the formation of the network-like structure was also related to the thermodynamic and kinetic factors during the solidification process of the molten pool. Additionally, the formation mechanism of the network-like structure would be analyzed from the melting stage, the flow stage and the solidification stage of the molten pool. The schematic diagram of the formation of the network-like structure is shown in Fig. 9.

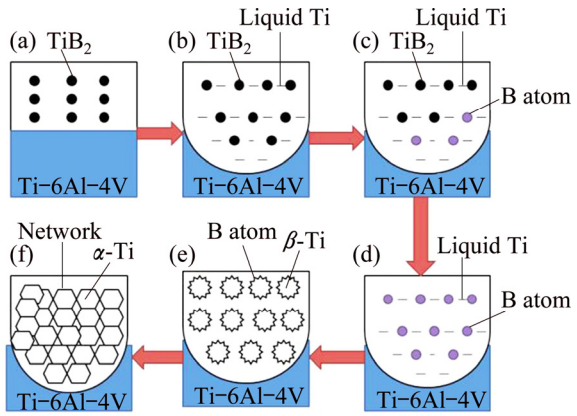


**Fig. 9** Schematic diagram of formation of network-like structure: (a) $TiB_2$ preset layer; (b) Initial stage of molten pool formation; (c) Dissolution of $TiB_2$ particle; (d) Formation of B atom; (e) Precipitation of $\beta$-Ti nuclei; (f) Formation of network-like structure

(1) Melting stage

$TiB_2$ particles were in the upper layer before laser irradiation (Fig. 9(a)), and the titanium alloy was in the bottom layer. Since the melting point (3253 °C) and the melting enthalpy (83.94 kJ/mol) of $TiB_2$ are high, the

$TiB_2$ particles were difficult to melt rapidly under the short-time laser irradiation. However, the titanium alloy in the lower layer was preferentially melted by heat transfer. Thus, the molten pool of Ti liquid was formed, which can be confirmed by the depression of the macro morphology of the cladding layer (Fig. 2(a)). In this process, the melting or the dissolution of $TiB_2$ particles depended mainly on the laser irradiation duration and the laser irradiation energy density. When the laser scanning speed was high or the laser power was low, a large amount of $TiB_2$ particles remained in the cladding layer, as shown in Figs. 7 and 8. In order to obtain the cladding layer with network-like structure, first it was necessary to eliminate $TiB_2$ particles in the cladding layer. With reducing the laser scanning speed or increasing the laser power, the in-situ reaction between $TiB_2$ and Ti can be improved, and thus, the $TiB_2$ particles in the cladding layer can be eliminated.

(2) Flow stage

Pure $TiB_2$ was used as a preset layer. Under laser irradiation, part of the substrate was melted by the heat conduction of the $TiB_2$ particles. In this case, the molten pool of Ti liquid was formed, and then the $TiB_2$ particles were continuously dissolved into the Ti liquid. In the initial stage of the molten pool formation, the $TiB_2$ particles were mainly in the upper layer, and the Ti liquid was mainly in the lower layer, as shown in Fig. 9(b). As a result, convection of the molten pool was generated under the action of temperature gradient and concentration gradient, leading to the continuous infiltration between Ti liquid and $TiB_2$ particles. Since the pre-coated layer of $TiB_2$ was directly irradiated by the laser, the activity of $TiB_2$ particles was promoted, which greatly improved the solubility of $TiB_2$ particles. In this process, the B atoms released by the dissolution of $TiB_2$ were dissolved in the Ti liquid and then diffused into the entire molten pool region, as shown in Figs. 9(c, d).

(3) Solidification stage

In the pre-coated layer, $TiB_2$ caused hypoeutectic concentration of B atoms during solidification of the molten pool, which led to precipitation of $\beta$-Ti core from the Ti liquid. Since the solid solubility of B in the Ti liquid was limited, the B solute would be released from the $\beta$-Ti core, which caused solute segregation around the boundaries of $\beta$-Ti phase, as shown in Fig. 9(e). Moreover, when B was enriched to a certain amount, TiB was formed by in-situ reaction with Ti. Meanwhile, TiB fine needles were spontaneously formed due to its unique B27 structure [28]. In addition, B was enriched at the boundaries of $\beta$-Ti phase, which would hinder the growth of $\beta$-Ti grain, resulting in grain refinement. In the meantime, $\beta$-Ti would be converted to $\alpha$-Ti during the cooling process, as shown in Fig. 9(f). The spatial length of the network-like structure gradually increased from the cladding layer surface to the interface. The reasons were as follows. On one hand, the content of Ti matrix at the bottom of the molten pool was larger than that of the surface of the molten pool due to the dilution of the substrate. On the other hand, the $TiB_2$ particle was in the upper layer and the liquid Ti was in the lower layer during the initial stage, and then the $TiB_2$ particles were continuously dissolved in the liquid. However, the duration of the molten pool was very short, so the content of the B element gradually decreased from the top to the bottom during the solidification process. Moreover, the core growth rate of $\beta$-Ti varied within the molten pool due to the effects of temperature gradient and concentration gradient.

According to the above analysis, the key to the formation of the network-like structure was the dissolution of $TiB_2$ particles and the priority precipitation of $\beta$-Ti core. Moreover, the dissolution of $TiB_2$ particles can be affected by the priority precipitation of $\beta$-Ti core. HU et al [16] also found that $\beta$-Ti nuclei were firstly formed/separated from the liquid and then grew into crystal grains during the formation process of the network structure. Therefore, the melting stage was very important for the formation of the network-like structure.

## 5 Properties of cladding layer

### 5.1 Mechanical properties

Figure 10 presents the results of the micro-hardness of the cladding layer with network-like structure. It was shown that the hardness of the top was the highest (649 $HV_{0.2}$), and it gradually decreased towards the interface. The hardness of the bottom was the lowest (572 $HV_{0.2}$). The average hardness of the cladding layer was about 614.5 $HV_{0.2}$. The hardness of the heat affected zone was low (426 $HV_{0.2}$), but it was higher than that of the substrate. The average hardness of the cladding layer was nearly 2 times higher than that of the substrate,

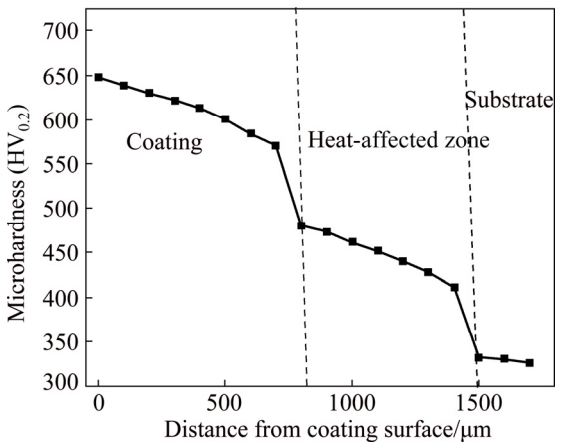


**Fig. 10** Micro-hardness of cladding layer with network-like structure

which was mainly due to the introduction of TiB strengthening phase and Ti grain refinement in the cladding layer. The amounts of strengthening phases and Ti grains were gradually reduced from the cladding layer surface to the bottom, which caused the highest hardness of the coating surface. Figure 11 shows the indentation morphologies of the cladding layer with network-like structure under the indentation load of 30 kg. No cracks were found, even in the four corner regions of the indentation, which indicated that the fracture toughness of the cladding layer can be improved by the introduction of the network-like structure.

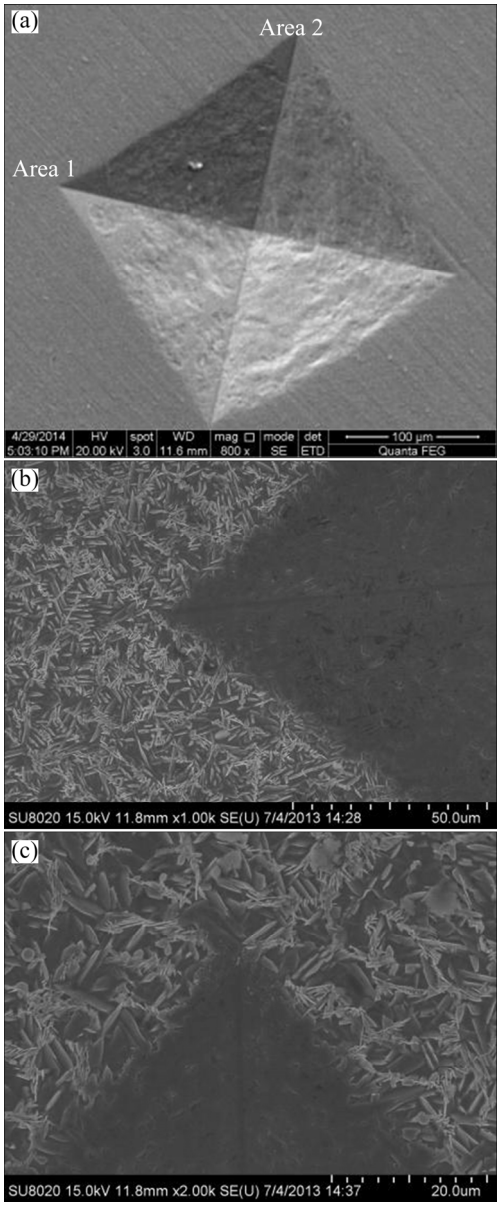


**Fig. 11** Morphology of indentation: (a) Overall appearance; (b) Area 1; (c) Area 2

### 5.2 Fretting wear performance

Fretting wear test was performed on the substrate and the cladding layer at room temperature. The results are given in Table 5. The contact zone of the cladding layer with the hardness of 612 $HV_{0.2}$ was selected as the research object and compared with the substrate. It can be seen that the micro-hardness of the cladding layer was nearly 2 times that of the substrate, but the friction coefficient of the cladding layer was only slightly lower than that of the substrate. Figure 12 illustrates the wear volume losses of the substrate and the cladding layer under different loads. It can be seen that the wear loss of the cladding layer was lower than that of the substrate under low load (50 and 100 N); however, the wear loss of the cladding layer was higher than that of the substrate under high load conditions (150 N).

**Table 5** Fretting wear test results of contact zone

| Type | Average micro-hardness ($HV_{0.2}$) | Average friction coefficient |
|---|---|---|
| Substrate | 330 | 0.55 |
| Coating | 612 | 0.49 |

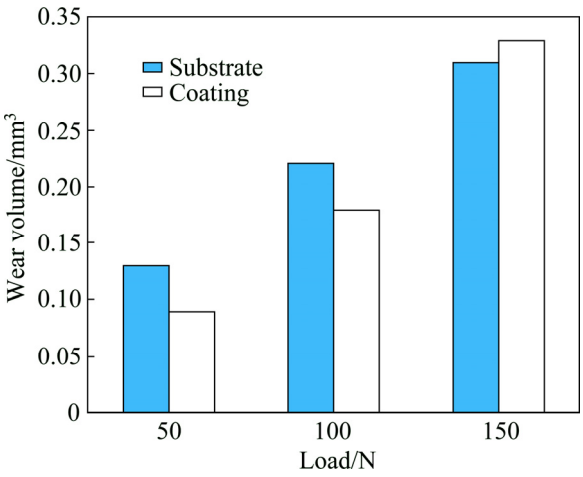


**Fig. 12** Wear volume of substrate and coating under different loads

To further investigate the fretting wear behavior of the network-like structure, the worn surfaces of the substrate and the cladding layer under 100 N load were examined using SEM. As shown in Fig. 13, adhesion pit occurred in the surface layer of the substrate, and the plough scars were obvious. On the contrary, the cladding layer had less wear scars and the amount of particle detachment was also reduced. By comparison, it was found that the depth of particle detachment on the surface of the cladding layer was less than that of the substrate. From observing the particle shedding behavior during the initial stage of fretting wear, multi-path crack bifurcation occurred during the crack propagation process, but the particle detachment on the worn surface of the cladding layer was not obvious, as shown in Fig. 14(a). However, crack propagation led to a closed loop during the continuous process of fretting wear,

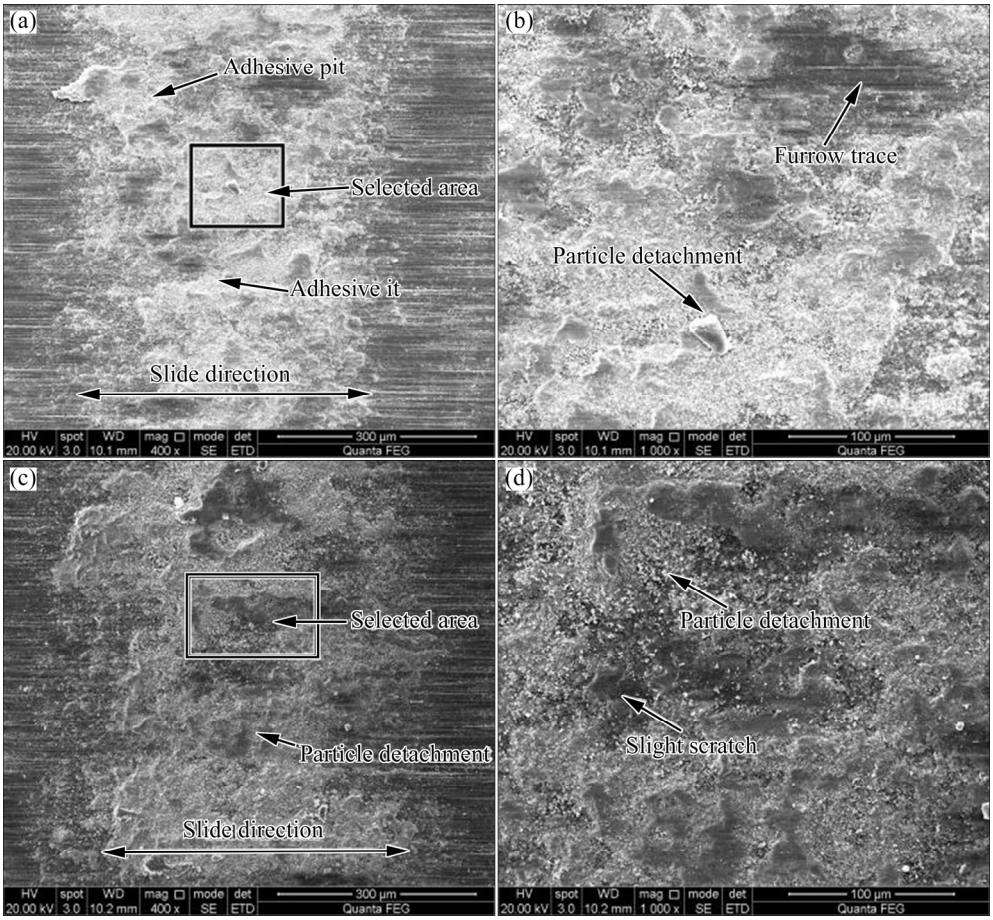


**Fig. 13** Wear scar morphologies of substrate (a, b) and cladding layer (c, d) under load of 100 N

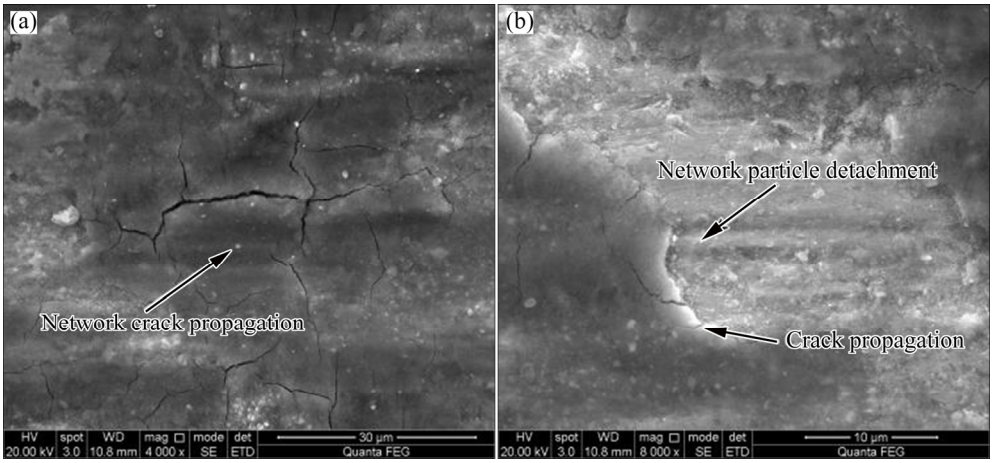


**Fig. 14** Particle detachment of cladding layer during fretting wear: (a) Reticular crack propagation at initial stage; (b) Particle detachment

resulting in particle detachment, as shown in Fig. 14(b). The Ti matrix of the cladding layer was not directly brought into contact by the introduction of the network-like structure during the fretting wear process. Moreover, the formation of TiB was mainly the process of laser in-situ synthesis, and thus, the interface bonding strength between the TiB and Ti matrix should be high. In this case, slipping of TiB short fibers may not occur during the fretting wear process, and TiB short fibers were removed only when they were fractured. The effects of TiB in the network-like structure can be the load sharing and reducing the contact area of the titanium matrix during the wear. Therefore, the network-like structure played a significant role in strengthening the matrix during the wear process, and protected the soft Ti matrix from damage.

## 6 Conclusions

(1) TiB−Ti network-like structure composite coating can be prepared via laser in-situ process on titanium alloy substrate with $TiB_2$ particles and appropriate process parameters. The key to the formation of the network-like structure was to eliminate residual $TiB_2$ particles in the cladding layer.

(2) The outer ring of the network-like structure was TiB strengthening phase, and the bonding interface between the TiB and the Ti matrix was very clean and had a constant orientation relationship; the inner ring of the network-like structure was mainly fine $\alpha$-Ti grains.

(3) The average hardness of the cladding layer with network-like structure was nearly 2 times that of the substrate, which was attributed to TiB strengthening, titanium grain refinement, solid solution strengthening and dislocation strengthening.

(4) Under low load (40 N), the fretting wear resistance of the cladding layer with network-like structure was larger than that of the substrate. The fretting wear mechanism was particle shedding caused by the formation of network-like crack closure.

## References


[1] GANGWAR K, RAMULU M. Friction stir welding of titanium alloys: A review [J]. Materials & Design, 2018, 141: 230−255.

[2] WU D, ZHANG L G, LIU L B, BAI W M, ZENG L J. Effect of Fe content on microstructures and properties of Ti6Al4V alloy with combinatorial approach [J]. Transactions of Nonferrous Metals Society of China, 2018, 28: 1714−1723.

[3] AN Q, HUANG L J, JIANG S, BAO Y, JI M, ZHANG R, GENG L. Two-scale TiB/Ti64 composite coating fabricated by two-step process [J]. Journal of Alloys and Compounds, 2018, 755: 29−40.

[4] GORSSE S, MIRACLE D B. Mechanical properties of Ti−6Al−4V/TiB composites with randomly oriented and aligned TiB reinforcements [J]. Acta Materialia, 2003, 51: 2472−2442.

[5] OZEROV M, KLIMOVA M, KOLESNIKOV A, STEPANOV N ZHEREBTSOV S. Deformation behavior and microstructure evolution of a Ti/TiB metal-matrix composite during high-temperature compression tests [J]. Materials & Design, 2016, 112: 17−26.

[6] LIN Y H, YAO J H, LEI Y P, FU H G, WANG L. Microstructure and properties of $TiB_2$−TiB reinforced titanium matrix composite coating by laser cladding [J]. Optics and Lasers in Engineering, 2016, 86: 216−227.

[7] TABRIZI S G, BABAKHANI A, SAJJADI S A, LIU W J. Microstructural aspects of in-situ TiB reinforced Ti−6Al−4V composite processed by spark plasma sin [J]. Transactions of Nonferrous Metals Society of China, 2015, 25: 1460−1467.

[8] HUANG L J, GENG L, PENG H X. Microstructurally inhomogeneous composites: Is a homogeneous reinforcement distribution optimal? [J]. Progress in Materials Science, 2015, 71: 93−168.

[9] ZHANG R, WANG D J, HUANG L J, YUAN S J, GENG L. Deformation behaviors and microstructure evolution of TiBw/TA15 composite with novel network architecture [J]. Journal of Alloys and Compounds, 2017, 722: 970−980.

[10] CAI A H, DING D W, AN W K, ZHOU G J, LUO Y, LI J H, PENG Y Y. Transition of plasticity and fracture mode of Zr−Al−Ni−Cu bulk metallic glasses with network structures [J]. Transactions of Nonferrous Metals Society of China, 2015, 25: 2617−2623.

[11] WANG S, HUANG L J, AN Q, GENG L, LIU B X. Dramatically enhanced impact toughness of two-scale laminate-network structured composites [J]. Materials & Design, 2018, 140: 163−171.

[12] ZHAO X N, LI H J, XU Z W, LI K Z, CAO S, JIANG G Z. Selective preparation and characterization of nano-hydroxyapatite/collagen coatings with three-dimensional network structure [J]. Surface and Coatings Technology, 2017, 322: 227−237.

[13] HU H T, HUANG L J, GENG L, LIU B X, WANG B. Oxidation behavior of TiB-whisker-reinforced Ti60 alloy composites with three-dimensional network architecture [J]. Corrosion Science, 2014, 85: 7−14.

[14] ZHOU Z Y, LIU X B, ZHUANG S G, WANG M, LUO Y S, TU R, ZHOU S F. Laser in-situ synthesizing $Ti_5Si_3$/$Al_3Ni_2$ reinforced $Al_3Ti$/NiTi composite coatings: Microstructure, mechanical characteristics and oxidation behavior [J]. Optics and Laser Technology, 2019, 109: 99−109.

[15] YANG M S, LIU X B, FAN J W. Microstructure and wear behaviors of laser clad Ni/$Cr_3C_2$−$WS_2$ high temperature self-lubricant wear-resistant composite coating [J]. Applied Surface Science, 2012, 258: 3757−3762.

[16] HU Y B, ZHAO B, NING F D, WANG H, CONG W L. In-situ ultrafine three-dimensional quasi-continuous network microstructural TiB reinforced titanium matrix composites fabrication using laser engineered net shaping [J]. Materials Letters, 2017, 195: 116−119.

[17] FU B G, WANG H W, ZOU C M, WEI Z J. Microstructural characterization of in situ synthesized TiB in cast Ti-1100−0.10B alloy [J]. Transactions of Nonferrous Metals Society of China, 2015, 25: 2206−2213.

[18] ZENG X, YAMAGUCHI T, NISHIO K. Characteristics of Ti(C,N)/TiB composite layer on Ti−6Al−4V alloy produced by laser surface melting [J]. Optics & Laser Technology, 2016, 80: 84−91.

[19] TAO X W, YAO Z J, ZHANG S S. Reconstruction and refinement of TiB whiskers in titanium matrix composite after electron beam remelting [J]. Materials Letters, 2018, 225: 13−16.

[20] ZHANG Y F, LI Z W, LI C G, YU Z S. Temperature gradient field sintering of Ti−TiB−$TiB_2$ functionally graded material [J]. Ceramics International, 2015, 41: 13844−13849.

[21] SATHEESH S M, BANERJEE A, BHATTACHARYA E. Determination of polysilicon Weibull parameters from indentation fracture [J]. Thin Solid Films, 2017, 642: 76−81.

[22] KOOI B J, PEI Y T, HOSSON J T M D. The evolution of microstructure in a laser clad TiB−Ti composite coating [J]. Acta Materialia, 2003, 51: 831−845.

[23] HUANG L Q, WANG L H,QIAN M, ZOU J. High tensile-strength and ductile titanium matrix composites strengthened by TiB nanowires [J]. Scripta Materialia, 2017, 141: 133−137.

[24] RAHOMA H K S, WANG X P, KONG F T, CHEN Y Y, HAN J C, DERRADJI M. Effect of ($\alpha$+$\beta$) heat treatment on microstructure and mechanical properties of (TiB+TiC)/Ti−B20 matrix composite [J]. Materials & Design, 2015, 87: 488−494.

[25] YANG S L, XIAO G Q, DING D H, REN Y, LV L H, YANG P. Dissolution-precipitation mechanism of combustion synthesis of

calcium aluminate [J]. Ceramics International, 2017, 43: 15918−15926.

[26] LIU X B, MENG X J, LIU H Q. Development and characterization of laser clad high temperature self-lubricating wear resistant composite coatings on Ti−6Al−4V alloy [J]. Materials and Design, 2014, 55: 404−409.

[27] LIN Y H, LEI Y P, LI X Q, ZHI X H, FU H G. A study of $TiB_2$/TiB gradient coating by laser cladding on titanium alloy [J]. Optics and Lasers in Engineering, 2016, 82: 48−55.

[28] FENG H B, ZHOU Y, JIA D C, MENG Q C. Stacking faults formation mechanism of in situ synthesized TiB whiskers [J]. Scripta Materialia, 2006, 55: 667−670.

# 激光原位制备 TiB−Ti 网状结构增强钛基复合涂层

林英华[1]，林振衡[1]，陈庆堂[1]，雷永平[1,2]，符寒光[2]

1. 莆田学院 机电工程学院，莆田 351100；
2. 北京工业大学 材料科学与工程学院，北京 100124

**摘　要：**针对激光熔覆凝固制备 TiB−Ti 复合涂层裂纹敏感性大的问题，以 $TiB_2$ 粉作为熔覆材料，利用激光原位技术在钛合金表面制备网状结构增强钛基复合涂层。采用 SEM、XRD、EPMA、TEM、硬度计和微动磨损仪对合成的钛基复合涂层进行测试和分析。结果表明，网状结构外部主要为 TiB 强化相，并与 Ti 基体界面之间结合洁净，具有固定的取向关系；网状结构内部主要为 $\alpha$-Ti 晶粒，且尺寸细小。网状结构熔覆层自表及里显微硬度逐渐降低，但平均显微硬度近基材的 2 倍。微动磨损测试显示，较低载荷下，网状结构熔覆层的耐磨性能优于基材。结果表明，类网状结构可以提高钛基复合涂层的硬度和抗微动磨损性能。

**关键词：**激光熔覆成形；钛基复合涂层；TiB−Ti；微动磨损

**(Edited by Bing YANG)**